



Comparisons between an on-axis three-mirror anastigmat telescope and an off-axis one: polarization aberrations

JING LUO,* CHENXU YOU, XU HE, AND XIAOHUI ZHANG

Changchun Institute of Optics, Fine Mechanics and Physics, Chinese Academy of Science, Changchun, Jilin 130033, China

*Corresponding author: luojingopt@ciomp.ac.cn

Received 20 May 2021; revised 23 June 2021; accepted 24 June 2021; posted 25 June 2021 (Doc. ID 432016); published 22 July 2021

Due to the ability to achieve a wide-diffraction-limited field of view, three-mirror anastigmat (TMA) telescopes are widely used in many applications that demand high imaging quality and detection accuracy, in which polarization aberrations play increasingly important roles. In this paper, polarization properties of on-axis elements and those of off-axis elements are analyzed and compared via polarization aberration theory. Then, an on-axis TMA (OTMA) telescope and an off-axis TMA (FTMA) telescope are designed and optimized to be diffraction-limited systems in parallel. Their constructional parameters and first-order parameters are set to be identical. Via polarization ray tracing, polarization aberrations of the 2 telescopes are obtained and compared in terms of diattenuation map, retardance map, Jones pupil, Pauli pupil, and amplitude response matrix. Results demonstrate that polarization aberrations are closely related to the structural features of mirrors and telescopes. The diattenuation and retardance maps of power mirrors in the OTMA telescope are rotationally symmetric, while those in the FTMA telescope are not. A Maltese cross appears in off-diagonal elements of the Jones pupil of the OTMA telescope and disappears in the FTMA telescope. Amplitude response matrices of polarization crosstalk components in the OTMA telescope are with a four-peak structure, while those in the FTMA telescope are with a two-peak structure. After quantitative comparisons, it is found that diattenuation in the OTMA telescope is smaller than that in the FTMA telescope as well as in the cases of retardance and polarization crosstalk. There are also similarities between the 2 TMA telescopes. Polarization aberrations of secondary mirrors (SM) are greater than those of both primary mirrors (PM) and tertiary mirrors (TM). What is more, polarization aberrations of TM are so small that they can be ignored safely. The numerical sum of Pauli coefficients of PM, SM, and TM is nearly identical to the cumulative Pauli coefficients. Hence, the TMA telescopes can be treated as weak polarization elements. This work compares polarization aberration performance of on- and off-axis TMA telescopes and can provide important references for designing and optimizing telescopes in which polarization aberrations matter. © 2021 Optical Society of America

<https://doi.org/10.1364/AO.432016>

1. INTRODUCTION

With several critical advantages such as wide-diffraction-limited field of view (FOV), good ability to control stray light and stray heat, real exit pupil, and compact structure design, three-mirror anastigmat (TMA) telescopes [1,2] become competent candidates in astronomical observations [3–6], space investigation cameras [7], remote sensing [8], and so on. TMA telescopes include on-axis TMA (OTMA) telescopes, whose primary mirror (PM) is partially obstructed by a secondary mirror (SM), and off-axis TMA (FTMA) telescopes in which SMs are off-set from the path of incoming light so that no obstruction is present. Both types of TMA telescopes are widely used. JWST [4], Euclid space telescopes [3], and SNAP [9] are OTMA telescopes; the HabEx space telescope [10], SPICES [11], WFIRST-A [12], and CSST [5] belong to FTMA telescopes.

Several superiorities and shortcomings of OTMA telescopes relative to FTMA telescopes have been well characterized and compared carefully in terms of wavefront errors, point spread function (PSF) [13,14], stray light control [15], and scattered light characteristics [16]. However, to the best of our knowledge, differences between their polarization aberrations have not been studied.

Polarization aberrations indicate the variations of amplitude, phase, and polarization associated with ray paths through optical systems [17]. Polarization aberrations occur at each reflecting and refracting surface due to the differences between reflectance and transmission coefficients of different polarization components. Compared with wavefront aberrations, the impacts of polarization aberrations on imaging quality are so small that they can be ignored safely in many optical systems. However, for applications that demand ultrahigh imaging quality or

detection accuracy such as photolithographic imaging [18], polarimeter measurements [19], astronomical remote sensing [20], and coronagraphs [21], polarization aberrations become important error sources. Effects of polarization aberrations on the PSF of astronomical telescopes have been analyzed in detail by Breckinridge *et al.* [22]. Chipman [23] and Davis [24] studied polarization aberrations in coronagraphs. Reference [25] pointed out that polarization aberrations of telescopes have nonignorable impacts on PSF ellipticity, which is a critical parameter for detecting weak gravitational lensing. In addition, polarization issues have attracted attention in several large aperture telescopes, such as the Thirty Meter Telescope [26], European Extremely Large Telescope [27], and WFIRST [28].

Polarization between on- and off-axis telescopes has been compared by Tran [29]. However, Ritchey–Cretien telescopes instead of TMA telescopes are analyzed, and only cross-polar performance is involved. On the one hand, polarization properties include diattenuation, retardance, Jones pupil, and amplitude response matrix besides polarization crosstalk. On the other hand, the effects caused by polarization aberrations vary by orders of magnitude between different types of telescopes [30]. In fact, polarization aberrations have become important considerations in choosing preferable structure types of telescopes. LUVOIR is a next-generation space telescope proposed by NASA with the primary mission of detecting and characterizing planetary systems around nearby stars [31]. To achieve better high-contrast imaging performance, research has been done to choose an optimal telescope scheme for LUVOIR [32]. OTMA and FTMA telescopes are 2 strong candidates. Their own advantages and disadvantages in many ways are compared carefully. Polarization has important impacts on coronagraph contrast so that it becomes one of the critical design considerations to LUVOIR priorities [32]. Hence, it is necessary to systematically compare OTMA telescopes with FTMA telescopes in terms of polarization aberrations.

In this paper, we focus on polarization aberrations in TMA telescopes. First, on- and off-axis optical elements are analyzed and compared via polarization aberration theory in Section 2. In Section 3, OTMA and FTMA telescopes are designed and optimized in parallel so that the main parameters of the 2 telescopes are set to be identical. Subsequently, diattenuation maps of mirrors in the 2 telescopes are obtained and compared, together with the retardance map, Jones pupil, Pauli pupil, and amplitude response matrix in Section 4. Finally, important discussions are analyzed and conclusions are summarized in Section 5.

2. POLARIZATION ABERRATIONS OF ON- AND OFF-AXIS OPTICAL ELEMENTS

The differences between on- and off-axis telescopes are partly embodied by on- and off-axis optical elements. Hence, we first analyze and compare polarization aberrations of on- and off-axis optical elements in this section.

Polarization aberrations in mirrors coated with homogeneous and isotropic material are characterized by the Fresnel formulae. The parallel (*P*-polarized light) and vertical polarization components (*S*-polarized light) of a light ray obliquely incident onto a mirror are characterized by

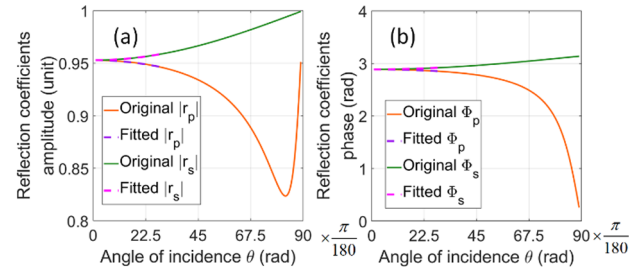


Fig. 1. Reflection coefficients for (a) amplitude and (b) phase of r_p and r_s at different angles of incidence.

Table 1. Fitting Results of Reflection Coefficients

Reflection Coefficients	Constant Parameter	Quadratic Parameter
$ r_p $	0.953	-0.0256
$ r_s $	0.953	0.0229
$ \Phi_p $	2.887	-0.142
$ \Phi_s $	2.887	0.125

$$\begin{cases} r_p = \frac{n^2 \cos \theta - \sqrt{n^2 - \sin^2 \theta}}{n^2 \cos \theta + \sqrt{n^2 - \sin^2 \theta}} = |r_p| \exp(i\Phi_p) \\ r_s = \frac{\cos \theta - \sqrt{n^2 - \sin^2 \theta}}{\cos \theta + \sqrt{n^2 - \sin^2 \theta}} = |r_s| \exp(i\Phi_s) \end{cases}, \quad (1)$$

where r_p is the reflective coefficient of *P*-polarized light and r_s is reflective coefficient of *S*-polarized light, n is the refractive index, θ indicates angle of incidence, and Φ_p and Φ_s are the phase variances of *P*- and *S*-polarized light, respectively.

If refractive index n of mirrors is chosen, as shown in Eq. (1), both r_p and r_s are only dependent on the angle of incidence θ . In this paper, all mirrors are coated with bare metal aluminum, whose refraction index is $1.45 + 7.54i$ at 632.8 nm [33]. The amplitude and phase of r_p and r_s at different incident angles are shown as solid lines in Figs. 1(a) and (b), respectively. In addition, the four curves are, respectively, fitted by quadratic functions when incident angles are smaller than 30 deg. Results are shown as dotted lines. The fitting coefficients are listed in Table 1. It can be found that both the amplitude and phase of r_p and r_s are fitted accurately. The maximal fitting errors of the amplitude and phase of r_p are $1.7e-4$ and $1.0e-3$, respectively, and the counterparts of r_s are $1.8e-4$ and $3.1e-5$.

Diattenuation and retardance are the 2 basic polarization properties of optical elements. Diattenuation D characterizes polarization-dependent reflectance

$$D = \frac{|r_s^2 - r_p^2|}{|r_s^2 + r_p^2|}. \quad (2)$$

The phase shift between the *S*- and *P*-polarized light is retardance

$$\delta = |\Phi_s - \Phi_p|. \quad (3)$$

Using Eqs. (1–3), the diattenuation and retardance of mirrors at different angles of incidence are shown as solid lines in Figs. 2(a) and 2(b), respectively. The maximum diattenuation is 0.007; the maximum retardance is 0.074. Evidently, they are so small that the mirror belongs to weak polarization elements

when angles of incidence are smaller than 30 deg (this would be proved strictly later) [30].

Similarly, the 2 solid curves in Fig. 2 are fitted with quadratic functions and shown as the dotted lines in Fig. 2. It can be seen that second-order fits are enough accurate. The maximal fitting errors of diattenuation and retardance are $9.2e-5$ and $1.1e-3$, respectively. Hence, polarization of the mirror can be analyzed by paraxial polarization aberrations [30].

According to the results shown in Figs. 1 and 2, we can see that, if angles of incidence are smaller than 30 deg, the mirrors coated with bare metal aluminum can be safely treated as weak polarization elements and analyzed by paraxial polarization aberrations. The fact is that angles of incidence in most TMA telescopes are smaller than 30 deg. Hence, polarization aberrations of TMA telescopes can be obtained by a greatly simplified method, i.e., Pauli representation. For weak polarization elements, its Jones matrix is characterized by [30]

$$\mathbf{J} \approx \rho_0 e^{-i\Phi_0} \left(\sigma_0 + \frac{D_H - i\delta_H}{2} \sigma_1 + \frac{D_{45} - i\delta_{45}}{2} \sigma_2 + \frac{D_L - i\delta_L}{2} \sigma_3 \right), \quad (4)$$

where σ_0 is the identity matrix, σ_i ($i = 1, 2, 3$) are Pauli spin matrices, and D_H and D_{45} indicate horizontal and 45 deg components of linear diattenuation, respectively. D_L is the circular diattenuation; δ_H , δ_{45} , and δ_L are mean corresponding retardance components. The Jones matrix of a mirror in its local coordinate system is predominantly related to linear diattenuation and retardance:

$$\mathbf{J}_0 \approx \rho_0 e^{-i\Phi_0} \left(\sigma_0 + \frac{D_H - i\delta_H}{2} \sigma_1 \right). \quad (5)$$

As noted, mirrors in TMA telescopes can be analyzed by paraxial polarization aberrations. Hence, the diattenuation and retardance are well approximated by quadratic functions. Equation (5) becomes

$$\mathbf{J}_0 \approx \rho_0 e^{-i\Phi_0} \left(\sigma_0 + \frac{D_2 \theta^2 - i\delta_2 \theta^2}{2} \sigma_1 \right), \quad (6)$$

where D_2 and δ_2 are the quadratic coefficients of diattenuation and retardance, respectively. In the global coordinate system, the Jones matrix becomes

$$\begin{aligned} \mathbf{J} &= \mathbf{R}(\varphi) \cdot \mathbf{J}_0 \cdot \mathbf{R}(-\varphi) \\ &\approx \rho_0 e^{-i\Phi_0} \cdot \left(\sigma_0 + \frac{D_2 \theta^2 - i\delta_2 \theta^2}{2} \cdot \cos(2\varphi) \sigma_1 \right. \\ &\quad \left. + \frac{D_2 \theta^2 - i\delta_2 \theta^2}{2} \cdot \sin(2\varphi) \sigma_2 \right), \end{aligned} \quad (7)$$

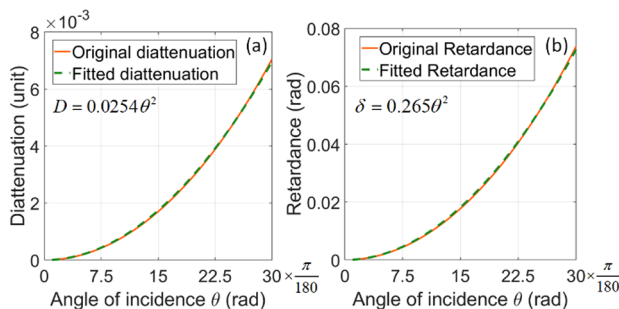


Fig. 2. (a) Diattenuation and (b) retardance of mirrors coated with bare metal aluminum at different angles of incidence.

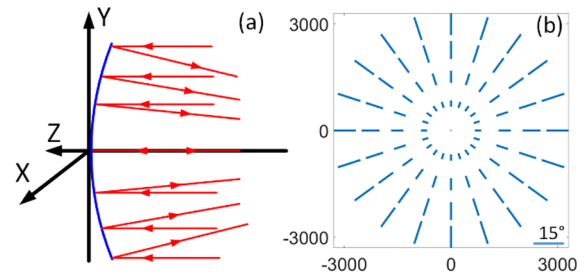


Fig. 3. (a) Parallel light rays are incident onto a paraboloid. (b) Map of angles of incidence and orientation of incident plane.

where φ is the angle between the local coordinate system and global coordinate system and is related to orientation of the incident plane. Horizontal (vertical) and 45 deg (135 deg) polarization aberration components are

$$\begin{cases} D_H = D_2 \theta^2 \cdot \cos(2\varphi) \\ \delta_H = \delta_2 \theta^2 \cdot \cos(2\varphi) \\ D_{45} = D_2 \theta^2 \cdot \sin(2\varphi) \\ \delta_{45} = \delta_2 \theta^2 \cdot \sin(2\varphi) \end{cases}. \quad (8)$$

According to Eq. (8), the polarization aberrations of mirrors depend on angles of incidence θ and orientation of incident plane φ across the beam. As shown in Fig. 3(a), parallel light rays are incident onto a paraboloid whose curvature radius of vertex is 10,000 mm and clear aperture is 5360 mm. Angles of incidence and orientation of the incident plane are mapped and shown in Fig. 3(b). The angle of incidence is 0 for the ray in the center of the pupil and increases linearly to marginal locations. The maximum angle of incidence is 15 deg. The incident plane is radially oriented.

Combining the results shown in Fig. 2 and Eq. (8), we can obtain the map of D_H and D_{45} of the paraboloid. Results are shown in Fig. 4. The map of δ_H and δ_{45} is similar to that in Fig. 4 but with different values. The global coordinate system is XOY , as shown in Fig. 4(a). An off-axis optical element is a part of the on-axis one. The offset of the geometric center of on-axis elements makes off-axis elements be nonrotationally symmetric. It is easy to find that the polarization aberrations of an on-axis optics element, as the circular A shown in Fig. 4(a), must be smaller than those of any off-axis one with the same clear aperture, marked as the circular B or C. The main reason is that D_H , D_{45} , δ_H , and δ_{45} are quadratic relation to angles of incidence θ , as shown by Eq. (8), and θ increases linearly along with the distance between the cross point and the central point O. Although polarization aberrations are also modulated by orientation of incident plane φ , the minimum value still locates at the on-axis position. Of course, synthetic diattenuation and retardance are independent of orientation of plane of incidence φ . Figure 4(b) shows the map of D_{45} , which is identical to Fig. 4(a) but rotates 45 deg.

Polarization crosstalk is a critical parameter, although it does not belong to basic polarization properties. Assuming that a horizontal linear polarization light ray is incident onto the paraboloid, the intensity of polarization crosstalk is

$$I_{90} = \frac{(D_2^2 + \delta_2^2)}{4} \cdot \theta^4 \cdot \sin^2(2\varphi). \quad (9)$$

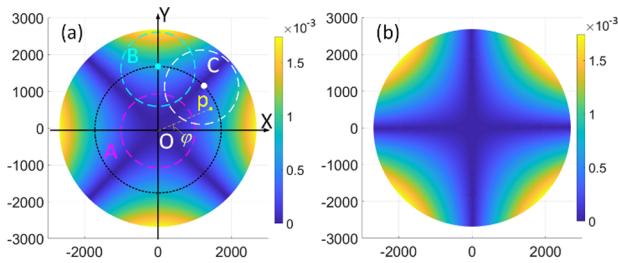


Fig. 4. Maps of (a) D_H and (b) D_{45} of the paraboloid.

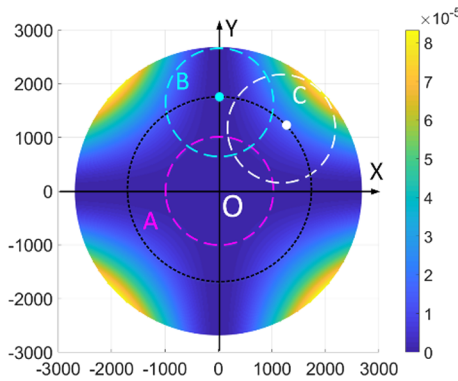


Fig. 5. Map of polarization crosstalk of the paraboloid.

The map of polarization crosstalk of the paraboloid is obtained. Results are shown in Fig. 5. Similarly, the polarization crosstalk of the on-axis optics element A is smaller than any off-axis one. For the horizontal linear polarization incident light ray, the maximum value of polarization crosstalk locates at 45 deg orientation. Both angles of incidence θ and orientation of plane of incidence φ have big influences on polarization crosstalk.

3. OTMA AND FTMA TELESCOPES

To compare the polarization aberrations of the 2 types of TMA telescopes, we modeled and optimized OTMA and FTMA telescopes in parallel, both having the same PM, effective focal length, and FOV, as shown in Fig. 6 and Table 2. In order to make the 2 telescopes be as similar and comparable as possible, the FTMA telescope is obtained from an unobstructed subaperture of the OTMA telescope. The OTMA telescope is scaled to produce the FTMA telescope with the desired aperture. The

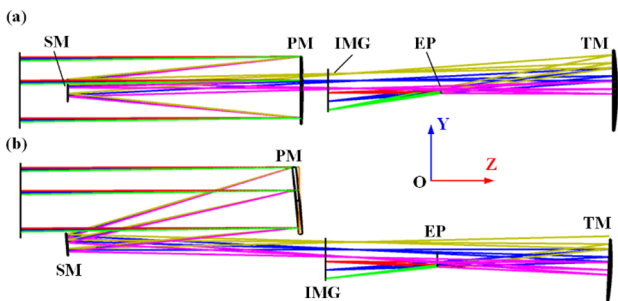


Fig. 6. (a) OTMA telescope. (b) FTMA telescope. PM, primary mirror; SM, secondary mirror; TM, tertiary mirror; EP, exit pupil plane; IMG, image plane.

Table 2. Primary Parameters of the OTMA and FTMA Telescopes

Specification	Value
Entrance pupil	PM
Entrance pupil diameter	1200 mm
Effective focal length	24543 mm
FOV	$0.787^\circ \times 0.709^\circ$
Coating	Aluminum

Table 3. Constructional Parameters of the OTMA Telescope

	Radius (mm)	Thickness (mm)	Decenter	Conic
STOP		5000	0	
PM	-10,800	-4140	0	-0.929
SM	-3339	9722	0	-2.108
TM	-4834	-3104.71	0	-0.425
EP		-2006.70	0	
IMG		0		

Table 4. Constructional Parameters of the FTMA Telescope

	Radius (mm)	Thickness (mm)	Decenter (mm)	Conic	Y-Decenter (mm)
STOP		5000	-1050		
PM	-10,800	-4140	0	-0.929	1050
SM	-3339	9722	0	-2.108	267
TM	-4834	-3104.71	0	-0.425	-218
EP		-2006.20	0		
IMG		0			

scale factor is chosen carefully to ensure that no ray incident onto the PM is obstructed by the SM and the tertiary mirror (TM). Detailed design and optimization process can be found in [14]. Constructional parameters of the 2 telescopes are listed in the Tables 3 and 4, respectively. The 2 telescopes are almost identical, except that Y-decenters of the apertures are different. Both of them are carefully designed to be diffraction-limited systems and achieve competent imaging performance in full FOVs.

4. POLARIZATION ABERRATIONS

In order to compare polarization aberrations of the 2 telescopes, we assume that they are all coated with metal aluminum whose complex index refraction is $n = 1.4482 + 7.5367i$ at 632.8 nm [33]. The polarization aberration theory used here is developed by Chipman and Breckinridge [22,30]. To comprehensively show and compare polarization aberrations of the 2 telescopes, the diattenuation map, retardance map, Jones pupil, Pauli pupil, and amplitude response matrix will be obtained successively.

A. Diattenuation Map

Diattenuation indicates that intensity transmittance of an element is a function of incident light polarization state. Hence, if unpolarized light, which is common for astronomical telescopes

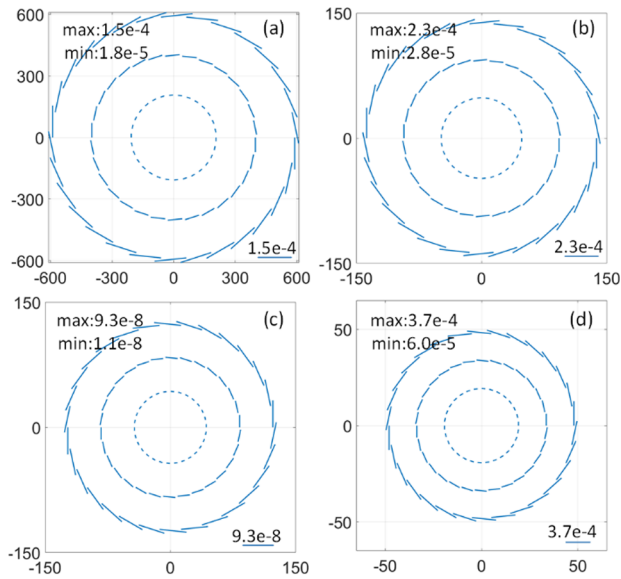


Fig. 7. Diattenuation maps of the (a) PM, (b) SM, (c) TM, and (d) the cumulative diattenuation for the whole OTMA telescope.

and can always be divided into 2 orthogonal polarization components, is received by telescopes with polarization aberrations, the intensities of 2 orthogonal polarization components in outgoing light will be different. As a result, unpolarized light becomes partially polarized.

Via polarization ray tracing [34,35], diattenuation map of each mirror in the OTMA telescope at the FOV of $[0^\circ, 0^\circ]$ is obtained and shown in Fig. 7. The length of each line is proportional to the diattenuation magnitude, and its orientation shows the axis of maximum transmission for a point in mirrors. Evidently, the diattenuation maps of all power mirrors PM, SM, and TM are rotationally symmetric. The maximum and minimum values of each diattenuation map are also shown in Fig. 7. The maximum diattenuation in the PM is slightly smaller than that in the SM, and both are far greater than that in the TM. The cumulative diattenuation in the EP for the whole OTMA telescope, which is also rotationally symmetric, is obtained and shown in Fig. 7(d).

Diattenuation maps of mirrors in the FTMA telescope at the FOV of $[0^\circ, 0^\circ]$ are obtained and shown in Fig. 8, which are very different from those shown in Fig. 7. The diattenuation maps of the three power mirrors in the FTMA telescope are no longer rotationally symmetric. This is easy to be understood because the PM, SM, and TM in the FTMA telescope are non-rotationally symmetric. The maximum diattenuation of the SM is greater than the counterparts of the other 2 mirrors. The cumulative diattenuation for the whole FTMA telescope is shown in Fig. 8(d); it is also nonrotationally symmetric.

To quantitatively compare diattenuation between the OTMA telescope and the FTMA telescope, we calculate the mean value of the diattenuation map of every mirror and cumulative diattenuation in the EP at different FOVs. Results are shown in Fig. 9, in which PST means the cumulative diattenuation of rays going through PM, SM, and TM [34,35], while Sum indicates the numerical sum of diattenuation of PM, SM, and TM. At each FOV, a diattenuation map that is similar to the

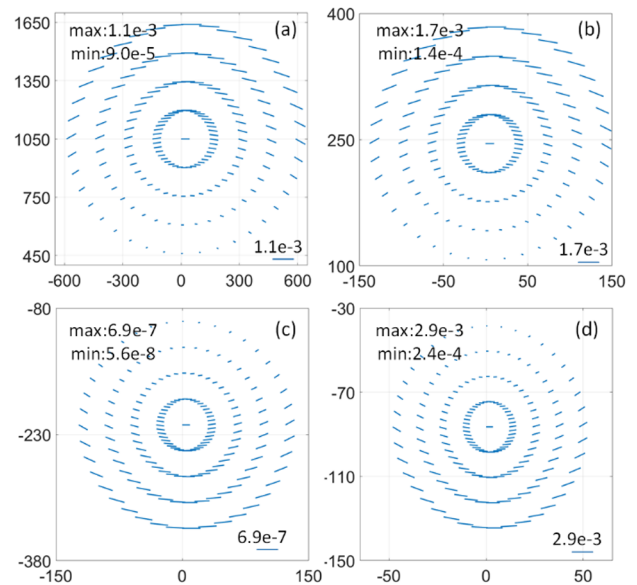


Fig. 8. Diattenuation maps of the (a) PM, (b) SM, (c) TM, and (d) the cumulative diattenuation for the whole FTMA telescope.

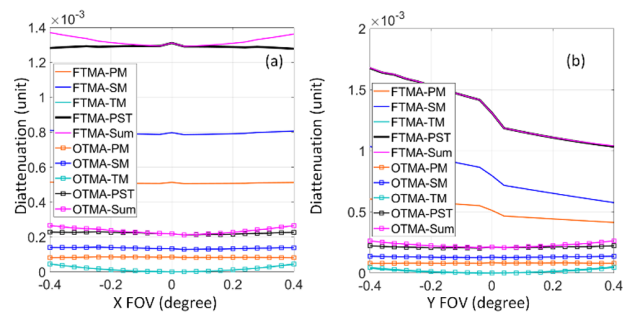


Fig. 9. Mean values of diattenuation maps at different (a) X-FOVs and (b) Y-FOVs in the OTMA telescope and the FTMA telescope.

results shown in Figs. 7 and 8 is obtained. For each diattenuation map, the mean value is calculated and picked out to represent its diattenuation performance. Twenty-one different FOVs are sampled over $[-0.4^\circ, 0.4^\circ]$ along X-FOVs and Y-FOV, respectively.

Obviously, diattenuations of the three mirrors in the FTMA telescope are greater than the counterparts in the OTMA telescope over both X-FOVs and Y-FOVs. The relationship between diattenuations of the PMs in the 2 telescopes is readily comprehensible and is provided in Section 2. However, polarization aberrations of the SMs and TMs are not apparent because light rays incident onto SMs are from PMs and are converging. Hence, polarization aberrations of the SMs and the TMs have to be obtained by polarization ray tracing, just as what has been done in Figs. 7–9.

Diattenuations of the three mirrors in one telescope are also compared. As shown in Fig. 9, diattenuations of the SMs in the 2 telescopes are greater than those of the PMs and TMs. What is more, diattenuations of the TMs are so small that they can be

ignored safely. The relative relationship among the diattenuations of PM, SM, and TM just embodies the characteristics of TMA telescopes very well.

The magenta curves and black curves in Fig. 9 are obtained by different ways. The magenta curves are the numerical sum of corresponding curves of PM, SM, and TM. As a contrast, the black curves indicate the cumulative diattenuation in which every light ray goes through PM, SM, and TM [34]. However, it can be seen that the magenta curves are almost identical to the black curves in the respective FOV and telescope. Differences between the 2 kinds of curves increase slowly, along with increasing FOVs. Particularly, the 2 curves match much better in the FTMA telescope at different Y-FOVs.

Diattenuation of the OTMA telescope increases slowly from 0° to $\pm 0.4^\circ$ FOV as well as the FTMA telescope at different X-FOVs. The case is different for diattenuation of the FTMA telescope at Y-FOVs, which keeps going down.

B. Retardance Map

When a light ray goes through an optical element, retardance characterizes that the phase variance of the light ray depends on its polarization state. Hence, if unpolarized light is received by a telescope, optical path differences of orthogonal polarization components are different. As a result, the whole wavefront in the image plane of telescopes would become fairly complicated [22]. Retardance maps for the three mirrors in the OTMA telescope at FOV of $[0^\circ, 0^\circ]$ are shown in Fig. 10. The length of each line is proportional to the value of retardance in radians, and its orientation shows fast axis. It should be noted that retardance results from geometric transformation has been removed [35]. The retardance maps of the PM, SM, and TM are rotationally symmetric. The maximum retardance of the SM is greater than that of the other 2 mirrors. The cumulative retardance map is shown in Fig. 10(d).

A retardance map for each mirror in the FTMA at FOV of $[0^\circ, 0^\circ]$ is shown in Fig. 11. As well as the diattenuation maps shown in Fig. 8, the retardance maps are also not rotationally

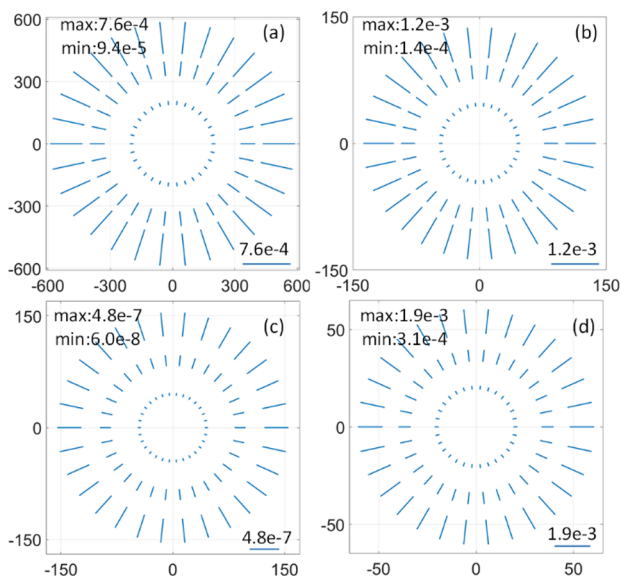


Fig. 10. Retardance maps of (a) the PM, (b) SM, (c) TM, and (d) cumulative retardance for the whole OTMA telescope.

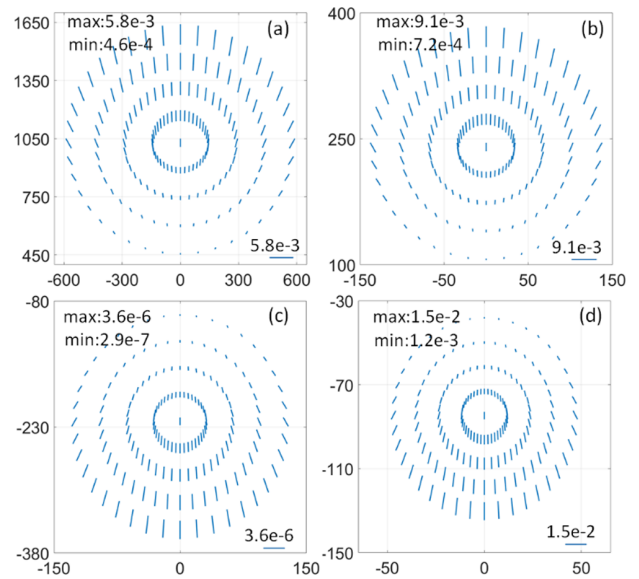


Fig. 11. Retardance maps of (a) the PM, (b) SM, (c) TM, and (d) cumulative retardance for the whole FTMA.

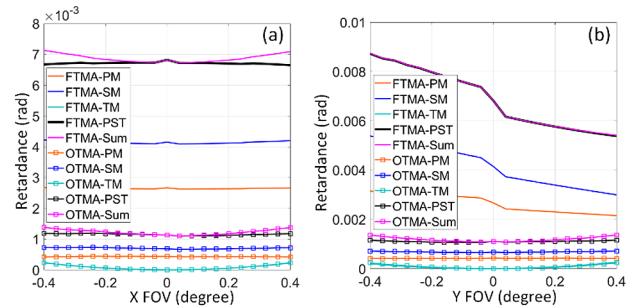


Fig. 12. Mean values of retardance maps in different (a) X-FOVs and (b) Y-FOVs in the OTMA telescope and the FTMA telescope.

symmetric. To compare retardance of the FTMA with that of the OTMA, the mean values of retardance maps at different FOVs are obtained, and the results are shown in Fig. 12. The calculation methods and comparison rules are identical to those in Fig. 9.

Combining the results shown in Figs. 9 and 12, we can see that the curves of retardance of the 2 telescopes are similar to the curves of diattenuation but with different values. The reason is shown in Fig. 2; both diattenuation and retardance are quadratic functions of incident angles but with different coefficients.

C. Jones Pupil

Jones matrices can fully characterize polarization properties of any element except depolarization. Mirrors in telescopes belong to ultrasmooth surfaces, whose depolarization can be safely ignored [30]. Hence, polarization aberrations of telescopes are usually characterized by Jones matrices. Each ray through an optical system has an associated Jones matrix. The polarization aberration function is a set of Jones matrices expressed as a function of the pupil and object coordinates. The set of Jones matrices for a specified object point is called the Jones pupil,

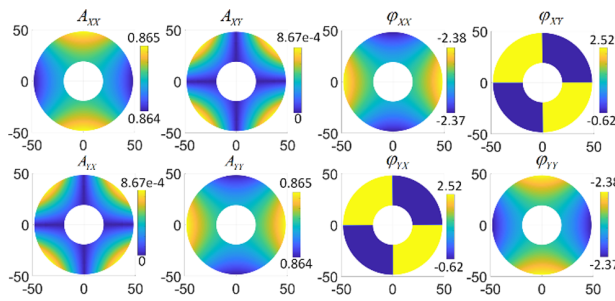


Fig. 13. Values of the Jones pupil elements of the OTMA telescope.

which has the form of a cumulative Jones matrix map over the whole telescopes in EP. The Jones pupil is represented by a set of 2×2 Jones matrices and contains complex components with amplitude and phase:

$$J(x, y) = \begin{bmatrix} J_{XX}(x, y) & J_{XY}(x, y) \\ J_{YX}(x, y) & J_{YY}(x, y) \end{bmatrix} \\ = \begin{bmatrix} A_{XX}(x, y) e^{i\varphi_{XX}(x, y)} & A_{XY}(x, y) e^{i\varphi_{XY}(x, y)} \\ A_{YX}(x, y) e^{i\varphi_{YX}(x, y)} & A_{YY}(x, y) e^{i\varphi_{YY}(x, y)} \end{bmatrix}, \quad (10)$$

where (x, y) is the coordinate of the intersection point of ray and EP. According to the definition of a Jones matrix, the meanings of each A and φ in Eq. (10) are apparent and will not be repeated here.

Via polarization ray tracing, the Jones pupil of the OTMA telescope is obtained and shown in Fig. 13. Every element in Eq. (10) is shown as a subgraph. The central hole in every subgraph is caused by the obstructed optical path in the OTMA telescope. On the whole, the Jones pupil is close to the identity matrix. Small deviations from the identity matrix occur due to polarization aberrations. The values of A_{XX} and A_{YY} are smaller than 1 because of reflection losses from mirror coatings. The off-diagonal elements A_{XY} and A_{YX} indicate polarization coupling or polarization crosstalk, whose values are evidently smaller than the diagonal elements. Both A_{XY} and A_{YX} are highly apodized, and typical Maltese cross patterns appear.

The phases of the diagonal elements φ_{XX} and φ_{YY} are continuously changing. As a contrast, the off-diagonal elements φ_{XY} and φ_{YX} change discontinuously because phase of a complex number changes by π when amplitude passes through 0, which is determined by Snell's law. The maximum and minimum values of A_{XX} are identical to those of A_{YY} as well as the case of φ_{XX} and φ_{YY} , which is different from those of other telescopes [20,22]. Hence, orthogonal polarization components of unpolarized sources going through the OTMA telescope would suffer from the same amplitude and phase variations. Of course, if plane mirrors are included as the cases of usual TMA telescopes, amplitude differences and wavefront differences would appear.

Every Jones matrix in the Jones pupil shown in Fig. 13 can be decomposed into Pauli matrices and the identity matrix [30,36]. Amplitude and phase of the four coefficients d_0 , d_1 , d_2 , and d_3 are shown in Fig. 14. It can be seen that circular diattenuation and circular retardance (d_3) are so small that they can be ignored. Primary polarization aberrations of the OTMA telescope are linear diattenuation and linear retardance. The maximum value of

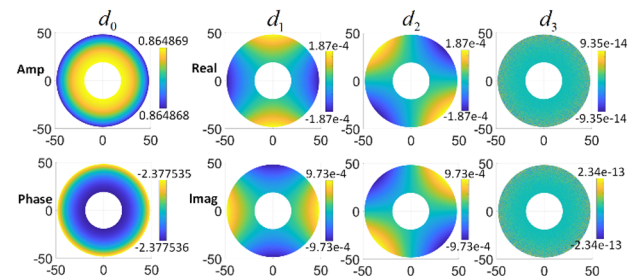


Fig. 14. Values of Pauli coefficient pupil of the OTMA telescope.

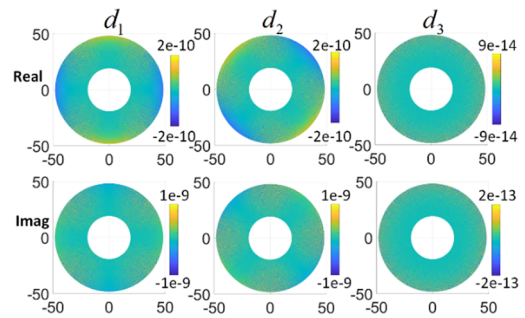


Fig. 15. Differences between the Pauli pupil and the numerical sum of Pauli coefficient maps of the PM, SM, and TM in the OTMA telescope.

horizontal component (d_1) of linear diattenuation is identical to that of 45 deg component (d_2) but occurs at different locations in the EP. It should be noted that all elements are continuous in Fig. 14, which are very different from the discontinuous elements φ_{XY} and φ_{YX} shown in Fig. 13. This is an important superiority of Pauli representation [36].

Figures 9 and 12 show the differences between the numerical sum of polarization aberrations and the cumulative polarization aberrations of PM, SM, and TM. In this section, we will show similar differences of the Pauli coefficients. In Fig. 14, the Pauli coefficients are obtained from the cumulative Jones matrices of the OTMA telescope. Via polarization ray tracing, we can also obtain the Jones matrix map for the PM, SM, and TM, respectively. Corresponding Pauli coefficient maps can be obtained for the three mirrors. Then, it is easy to obtain the numerical sum of Pauli coefficients of the three mirrors. In this way, the differences between the numerical sum of Pauli coefficients and the cumulative Pauli coefficients are obtained and shown in Fig. 15. The differences of all elements are so small that they can be ignored. Hence, the OTMA telescope is a truly weak polarization system.

The Jones pupil of the FTMA telescope is shown in Fig. 16. There are also big differences between the results shown in Fig. 13 and those in Fig. 16. Due to the unobstructed optical path of the FTMA telescope, holes in the center disappear. Polarization crosstalk elements A_{XY} and A_{YX} in Fig. 16 are much greater than the counterparts in Fig. 13. In addition, a Maltese cross pattern disappears in both A_{XY} and A_{YX} of the FTMA telescope. The phases of polarization crosstalk φ_{XY} and φ_{YX} also change discontinuously and jump twice in a ring, while those jump four times in the OTMA telescope.

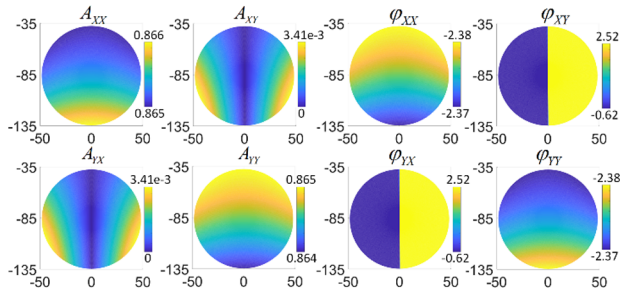


Fig. 16. Values of the Jones pupil elements of the FTMA telescope.

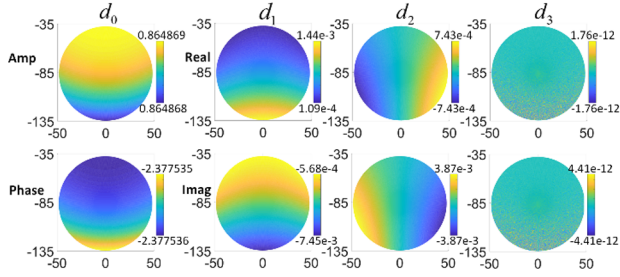


Fig. 17. Values of Pauli coefficient pupil of the FTMA telescope.

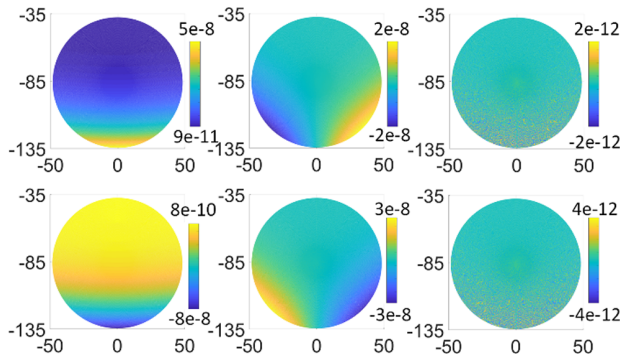


Fig. 18. Differences between the Pauli pupil and the sum of Pauli maps of the PM, SM, and TM in the FTMA telescope.

Similarly, the Jones pupil in Fig. 16 is decomposed into Pauli matrices and the identity matrix. Results are shown in Fig. 17. Linear polarization aberrations are dominant, while circular polarizations can also be ignored safely. Being different from the OTMA telescope, the maximum value of horizontal component (d_1) of linear diattenuation is greater than that of the 45 deg component (d_2) as well as the case of linear retardance (absolute value).

In the same way, the differences between the numerical sum and the cumulative Pauli coefficients of the FTMA telescope are obtained and shown in Fig. 18. It can be seen that the FTMA telescope is also a weak polarization system.

D. Amplitude Response Matrix

The amplitude response matrix (ARM) is obtained by Fourier transform of each element of the Jones pupil:

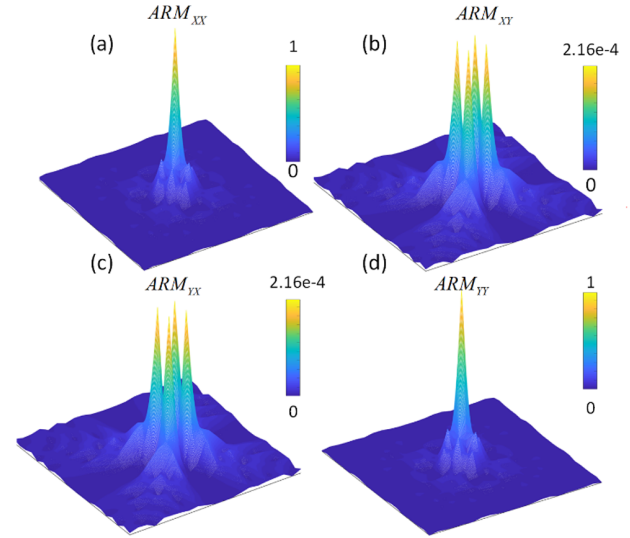


Fig. 19. Values of the ARM of the OTMA telescope.

$$ARM = \begin{bmatrix} F[U_{XX}(x, y)] & F[U_{XY}(x, y)] \\ F[U_{YX}(x, y)] & F[U_{YY}(x, y)] \end{bmatrix}, \quad (11)$$

where F means Fourier transform operator, and ARM is the matrix form of the amplitude response function.

Combining the results shown in Fig. 13 with Eq. (11), we can obtain the ARM of the OTMA telescope. Results are shown in Fig. 19, in which all elements are normalized by the maximum value of ARM_{XX} . Diagonal elements ARM_{XX} and ARM_{YY} are a typical Airy disk pattern in on-axis telescopes, whose PSFs are with considerable sidelobes because of the obscured SM. The maximum value of ARM_{XX} is identical to that of ARM_{YY} . Off-diagonal elements ARM_{XY} and ARM_{YX} show polarization crosstalk of the telescope and are also called a “ghost image” [22]. Due to polarization aberrations, ARM_{XY} and ARM_{YX} appear and are split into four components. According to the results shown in Fig. 19, the normalized amplitude of the polarization crosstalk component of the OTMA is $2.16e-4$. Polarization crosstalk of telescopes is troublesome in many applications, such as polarization remote-sensing lidars [19] and high-contrast coronagraphs for detecting exoplanets [24] and so on.

The ARM of the FTMA telescope is shown in Fig. 20. Thanks to the unobscured structure, the sidelobes of ARM_{XX} and ARM_{YY} in Fig. 20 are significantly smaller than those in Fig. 19. The off-diagonal elements ARM_{XY} and ARM_{YX} consist of 2 peaks rather than four peaks. The maximum values of ARM_{XY} and ARM_{YX} in Fig. 20 are relatively greater than those in Fig. 19, meaning that polarization crosstalk of the FTMA telescope is greater than that of the OTMA telescope. In addition, ARM_{XX} and ARM_{YY} are not identical in Fig. 20. The reason is explained in the last section.

Finally, it should be noted that the PSF of telescopes for an unpolarized source consists of four additive components, i.e., $I = |ARM_{XX}|^2 + |ARM_{XY}|^2 + |ARM_{YX}|^2 + |ARM_{YY}|^2$. As shown in Figs. 19 and 20, polarization crosstalk components, i.e., ARM_{XY} and ARM_{YX} , are with a multippeak structure. Hence, polarization aberrations would induce the spatial distribution of PSF to be complicated and no longer rotational symmetric [25]. This is critical to astronomical telescopes

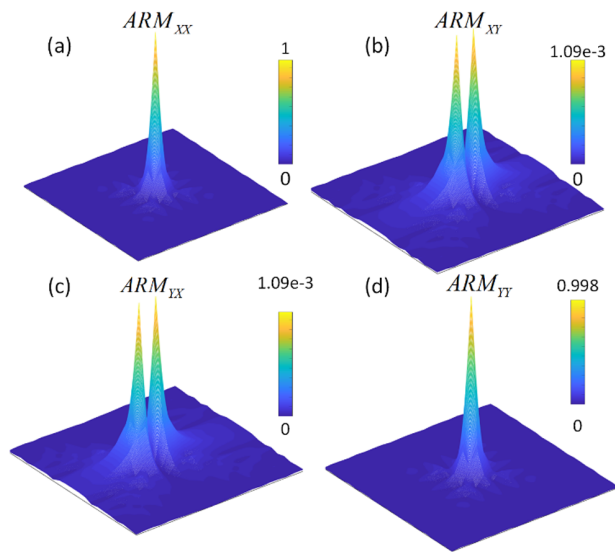


Fig. 20. Values of the ARM of the FTMA telescope.

such as the Euclid space telescope [3] and CSST [5], which aim to detect weak gravitational lensing, in which PSF ellipticity caused by telescopes is one of the most important systematic errors.

5. DISCUSSIONS AND CONCLUSIONS

TMA telescopes are widely used in many applications that demand high imaging quality and detection accuracy. In this paper, OTMA and FTMA telescopes are designed and optimized in parallel. Both are diffraction-limited systems and achieve good imaging performance in full FOVs. In order to make the 2 telescopes be as similar and comparable as possible, their constructional parameters, f -number, effective focal length, effective FOV, and coating film are set to be identical. Via polarization ray tracing, polarization aberrations of the 2 telescopes are obtained and compared in terms of diattenuation map, retardance map, Jones pupil, Pauli pupil, and amplitude response matrix. Discussions and conclusions are listed as follows:

1. Via polarization aberration theory, polarization properties of on- and off-axis optical elements are compared in terms of diattenuation, retardance, and polarization crosstalk. Due to smaller angles of incidence, polarization aberrations of on-axis elements are always smaller than those of other off-axis subapertures with the same diameter.
2. Polarization aberrations are closely related to structural features of telescopes. All power mirrors in the OTMA telescopes are rotationally symmetric about the optical axis, so that diattenuation and retardance maps of these mirrors are also rotationally symmetric. In contrast, diattenuation and retardance maps of the FTMA telescope are nonrotationally symmetric.
3. In OTMA and FTMA telescopes, the numerical sum of corresponding diattenuation of PM, SM, and TM is nearly identical to the cumulative diattenuation as well as the case of retardance. Similarly, the differences between numerical sum of Pauli coefficients and the cumulative

Pauli coefficients in the 2 telescopes are so small that they can be ignored safely. It is proved that TMA telescopes are weak polarization elements and can be analyzed by paraxial polarization aberrations. This is important because polarization aberrations of TMA telescopes can be obtained by a greatly simplified method, i.e., Pauli representation.

4. The cases of Jones pupil and ARM in the 2 telescopes are consistent with diattenuation and retardance. If unpolarized light goes through the OTMA telescope, orthogonal polarization components would suffer from identical amplitude and phase variations. For the FTMA telescope, however, incident unpolarized light becomes partially polarized light whose orthogonal polarization components are with different wavefront aberrations.
5. Diattenuation, retardance, and polarization crosstalk of power mirrors in the OTMA telescope are significantly smaller than the counterparts in the FTMA telescope. Evidently, this is one shortcoming of off-axis telescopes, although they have several other important advantages over on-axis ones.
6. Polarization aberrations of SMs in the OTMA and FTMA telescopes are greater than those of both PMs and TMs. What is more, polarization aberrations of TMs are so small that they can be safely ignored. The relative relationship among the polarization aberrations of PM, SM, and TM embodies the characteristics of TMA telescopes.
7. Plane mirrors, which are always used in TMA telescopes to adjust light path and focal planes, are not included in this paper. The reason is that plane mirrors enable one to change and compensate the polarization aberrations arising from upstream optical elements, which would disturb our comparisons in this paper.

Funding. National Natural Science Foundation of China (12003033, 61875190); ShuGuang Talents Scheme Award of Changchun Institute of Optics, Fine Mechanics and Physics, Chinese Academy of Sciences.

Disclosures. The authors declare no conflicts of interest.

Data Availability. Data underlying the results presented in this paper are not publicly available at this time but may be obtained from the authors upon reasonable request.

REFERENCES

1. D. Korsch, "Design and optimization technique for three-mirror telescopes," *Appl. Opt.* **19**, 3640–3645 (1980).
2. L. G. Cook, "Three-mirror anastigmat used off-axis in aperture and field," *Proc. SPIE* **183**, 207–211 (1979).
3. R. Laureijs, J. Amiaux, S. Arduini, J.-L. Augeres, J. Brinchmann, R. Cole, M. Cropper, C. Dabin, L. Duvet, and A. Ealet, "Euclid definition study report," arXiv:1110.3193 (2011).
4. P. A. Lightsey, C. B. Atkinson, M. C. Clampin, and L. D. Feinberg, "James Webb space telescope: large deployable cryogenic telescope in space," *Opt. Eng.* **51**, 0111003 (2012).
5. Y. Gong, X. W. Liu, Y. Cao, X. Chen, Z. Fan, R. Li, X. Li, Z. Li, X. Zhang, and H. Zhan, "Cosmology from the Chinese space station optical survey (CSS-OS)," *Astrophys. J.* **883**, 203 (2019).
6. D. M. Harrington and S. R. Sueoka, "Polarization modeling and predictions for Daniel K. Inouye Solar telescope part 1: telescope and example instrument configurations," *J. Astron. Telesc. Instrum. Syst.* **3**, 018002 (2017).
7. J. D. Mill, R. R. O'Neil, S. Price, G. J. Romick, O. Manuel, E. M. Gaposchkin, G. C. Light, W. W. Moore, T. L. Murdocka, and A. T. Stair,

- "Midcourse space experiment: introduction to the spacecraft, instruments, and scientific objectives," *J. Spacecr. Rockets* **31**, 900–907 (1994).
8. B. Sang, J. Schubert, S. Kaiser, V. Mogulsky, C. Neumann, K. P. Förster, S. Hofer, T. Stuffer, H. Kaufmann, and A. Müller, "The EnMAP hyperspectral imaging spectrometer: instrument concept, calibration, and technologies," *Proc. SPIE* **7086**, 708605 (2008).
 9. M. Lampton, C. Akerlof, G. Aldering, R. Amanullah, P. Astier, E. Barrelet, C. Bebek, L. Bergstrom, J. Bercovitz, G. Bernstein, M. Bester, A. Bonissant, C. Bower, W. Carithers, E. Commins, C. Day, S. Deustua, R. DiGennaro, A. Ealet, R. Ellis, M. Eriksson, A. Fruchter, J.-F. Genat, G. Goldhaber, A. Goobar, D. Groom, S. Harris, P. Harvey, H. Heetderks, S. Holland, D. Huterer, A. Karcher, A. Kim, W. Kolbe, B. Krieger, R. Lafever, J. Lamoureux, M. Levi, D. Levin, E. Linder, S. Loken, R. Malina, R. Massey, T. McKay, S. McKee, R. Miquel, E. Mortsell, N. Mostek, S. Mufson, J. Musser, P. Nugent, H. Oluseyi, R. Pain, N. Palaio, D. Pankow, S. Perlmutter, R. Pratt, E. Prieto, A. Refregier, J. Rhodes, K. Robinson, N. Roe, M. Sholl, M. Schubnell, G. Smadja, G. Smoot, A. Spadafora, G. Tarle, A. Tomasch, H. von der Lippe, R. Vincent, J.-P. Walder, and G. Wang, "SNAP telescope," *Proc. SPIE* **4849**, 215–226 (2002).
 10. J. Davis, M. K. Kupinski, R. A. Chipman, and J. B. Breckinridge, "HabEx polarization ray trace and aberration analysis," *Proc. SPIE* **10698**, 106983H (2018).
 11. A. Boccaletti, J. Schneider, W. Traub, P.-O. Lagage, D. Stam, R. Gratton, J. Trauger, K. Cahoy, F. Snik, and P. Baudoz, "SPICES: spectro-polarimetric imaging and characterization of exoplanetary systems from planetary disks to nearby Super Earths," *Exp. Astron.* **34**, 355–384 (2012).
 12. M. E. Levi, M. Lampton, A. G. Kim, and M. Sholl, "Science yield of an improved wide field infrared survey telescope (WFIRST)," arXiv: Instrumentation and Methods for Astrophysics (2011).
 13. M. L. Lampton, J. Oschmann, M. Jacobus, M. C. Clampin, M. J. Sholl, M. E. Levi, and H. A. MacEwen, "Off-axis telescopes for dark energy investigations," *Proc. SPIE* **7731**, 77311G (2010).
 14. B. Singaravelu and R. A. Cabanac, "Obstructed telescopes versus unobstructed telescopes for wide field survey—a quantitative analysis," *Publ. Astron. Soc. Pac.* **126**, 386 (2014).
 15. J. L. Stauder, *Stray Light Comparison of Off-Axis and On-Axis Telescopes* (Utah State University, 2000).
 16. J. Kuhn and S. Hawley, "Some astronomical performance advantages of off-axis telescopes," *Publ. Astron. Soc. Pac.* **111**, 601 (1999).
 17. R. A. Chipman, *Polarization Aberrations* (University of Arizona, 1987).
 18. J. Ruoff and M. Totzeck, "Orientation Zernike polynomials: a useful way to describe the polarization effects of optical imaging systems," *J. Micro/Nanolithogr., MEMS, MOEMS* **8**, 031404 (2009).
 19. J. Luo, D. Liu, Z. Huang, B. Wang, and L. Su, "Polarization properties of receiving telescopes in atmospheric remote sensing polarization lidars," *Appl. Opt.* **56**, 6837–6845 (2017).
 20. F. C. M. Bettonvil, M. Collados, A. Feller, B. F. Gelly, C. U. Keller, T. J. Kentischer, A. L. Ariste, O. Pleier, F. Snik, and H. Socas-Navarro, "The polarization optics for the European solar telescope (EST)," *Proc. SPIE* **7735**, 77356I (2010).
 21. S. D. Will and J. R. Fienup, "Effects and mitigation of polarization aberrations in LUVVOIR coronagraph," *Proc. SPIE* **11117**, 1111710 (2019).
 22. J. B. Breckinridge, W. S. T. Lam, and R. A. Chipman, "Polarization aberrations in astronomical telescopes: the point spread function," *Publ. Astron. Soc. Pac.* **127**, 445–468 (2015).
 23. R. A. Chipman, "Challenges in coronagraph optical design," *Proc. SPIE* **10374**, 1037403 (2017).
 24. J. M. Davis, *Polarization Aberrations in Coronagraphs* (The University of Arizona, 2019).
 25. J. Luo, X. He, K. Fan, and X. Zhang, "Effects of polarization aberrations in an unobscured off-axis space telescope on its PSF ellipticity," *Opt. Express* **28**, 37958–37970 (2020).
 26. R. M. Anche, A. K. Sen, G. C. Anupama, K. Sankarasubramanian, and W. Skidmore, "Analysis of polarization introduced due to the telescope optics of the thirty meter telescope," *J. Astron. Telesc. Instrum. Syst.* **4**, 018003 (2018).
 27. M. D. J. Ovelar, F. Snik, C. U. Keller, and L. Venema, "Instrumental polarisation at the Nasmyth focus of the E-ELT," *Astron. Astrophys.* **562**, A118–A130 (2014).
 28. J. E. Krist, B. Nemati, and B. P. Mennesson, "Numerical modeling of the proposed WFIRST-AFTA coronagraphs and their predicted performances," *J. Astron. Telesc. Instrum. Syst.* **2**, 011003 (2015).
 29. H. T. Tran, "Polarization comparison between on-axis and off-axis dual reflector telescopes: Zemax and Grasp8 simulations," *New Astron. Rev.* **47**, 1091–1096 (2003).
 30. R. A. Chipman, G. Young, and W. S. T. Lam, *Polarized Light and Optical Systems* (CRC press, 2018).
 31. J. Breckinridge, M. Kupinski, J. Davis, B. Daugherty, and R. Chipman, "Terrestrial exoplanet coronagraph image quality: study of polarization aberrations in Habex and LUVVOIR update," *Proc. SPIE* **10698**, 106981D (2018).
 32. M. R. Bolcar, *LUVVOIR Telescope Design Overview* (2016).
 33. A. D. Rakić, "Algorithm for the determination of intrinsic optical constants of metal films: application to aluminum," *Appl. Opt.* **34**, 4755–4767 (1995).
 34. G. Yun, K. Crabtree, and R. A. Chipman, "Three-dimensional polarization ray-tracing calculus I: definition and diattenuation," *Appl. Opt.* **50**, 2855–2865 (2011).
 35. G. Yun, S. C. McClain, and R. A. Chipman, "Three-dimensional polarization ray-tracing calculus II: retardance," *Appl. Opt.* **50**, 2866–2874 (2011).
 36. N. Yamamoto, J. Kye, and H. J. Levinson, "Polarization aberration analysis using Pauli-Zernike representation," *Proc. SPIE* **6520**, 65200Y (2007).